PHYSICAL REVIEW C **106**, 034003 (2022)

Effect of nuclear charge on laser-induced fusion enhancement in advanced fusion fuels

John Jasper Bekx [1,*] Martin Louis Lindsey,[2] and Karl-Georg Schlesinger[1]
[1]*Marvel Fusion, Theresienhöhe 12, 80339 Munich, Germany*
[2]*Institute for Computational & Mathematical Engineering, Stanford University, 475 Via Ortega, Stanford, California 94305, USA*

(Received 10 May 2022; accepted 19 September 2022; published 27 September 2022)

Based on the preliminary work done in a previous paper [Phys. Rev. C **105**, 054001 (2022)], we investigate the effects of laser-induced fusion rate enhancements of different fusion fuels. In the aforementioned work, which considered ${}^2_1$H - ${}^3_1$H (D-T) and DHe^3 fusion, it was observed that a larger product of charge numbers of the fusion reactants leads to an increased laser-induced enhancement to the fusion cross section for static external electric fields. We investigate whether this trend persists for DT, DHe^3, and pB^{11} fusion for dynamical electric fields, using the semiclassical approaches of the Wentzel-Kramers-Brillouin method and the imaginary-time method, as well as the Kramers-Henneberger method, and the Volkoff-state approximation. We find that the fusion cross section of pB^{11} indeed exhibits the largest relative enhancement for all laser parameters considered and may even surpass the cross section of DT and DHe^3 fusion.

DOI: 10.1103/PhysRevC.106.034003

I. INTRODUCTION

With recent newly achieved milestones in fusion research [1–3], the goal of using nuclear fusion as a clean sustainable source of energy is inching ever closer towards reality. These achievements notwithstanding, obtaining nuclear fusion ignition in the laboratory remains a challenging feat, which stands to benefit greatly from new ways that increase the fusion reaction rates. One such a possible avenue is the fusion cross-section enhancement from a high-power laser. The theoretical study of the effects of laser fields on fusion reactions is slowly beginning to establish itself as a new field in its own right [4–12], and the availability of high-power laser facilities [13–18] provides the possibility to design and perform experiments towards observing laser-induced fusion enhancement.

In a previous work [4], we investigated the effect of an electric field associated with an external laser on the DT and DHe^3 fusion reactions. D and T refer to the isotopes ${}^2_1$H and ${}^3_1$H, respectively. In particular, we analyzed the applicability of the frequently used semiclassical (SC) methods of the Wentzel-Kramers-Brillouin (WKB) approximation [19,20] and the imaginary-time method (ITM) [21] for a range of different laser parameters. When investigating the effects of a static electric field, we found that the laser-induced enhancement to the fusion cross section was larger for those reactions where the product of the charge numbers of the reactants was larger. This increased enhancement would be exceedingly beneficial for the pB^{11} fusion reaction, considering the relatively high charge state of the boron nucleus as compared with those of deuterium, tritium, or helium nuclei. Despite the lower reaction yield of pB^{11} fusion as compared with those of more conventional fuels such as DT and DHe^3, the consideration of pB^{11} as a fusion fuel has remained a relevant topic in the study towards commercialized fusion power. This is because the pB^{11} reaction provides several practical advantages [22]: the reaction is aneutronic, it results directly in the creation of charged α particles, and the relevant reactants are readily obtainable on Earth. Thus, even though the stronger Coulombic repulsion between the pB^{11} nuclei results in a reduced fusion yield, it may in turn lead to an increased laser-induced enhancement, potentially nearing or surpassing the fusion cross sections of conventional fuels. For this reason, we investigate whether this charge-number-increased laser-enhanced (CNILE) trend persists for dynamic electric fields as well.

As we concluded in Ref. [4] that the SC methods are only applicable for a limited range of laser parameters in the dynamic case, we invoke the Kramers-Henneberger (KH) method [23] to more reliably cover the phase space of dynamic laser parameters. In addition, we employ a fourth method, the Volkoff-state approximation (VSA) [24] for comparison. This method stands out from the other three because the interpretation behind the effect of the external laser field on the fusion process differs. Whereas the prior three methods interpret the laser-induced enhancement of the fusion rate as caused by a deformation to the interparticle Coulombic repulsion, the VSA interprets the enhancement as a result from the energy gain provided to the fusing system from the laser. We emphasize that this deformation and energy gain are not two distinct processes that occur, but are rather two different ways of interpreting the additional potential term that captures the behavior of the external laser field. The changes the laser field induces to the particle velocity distribution in an ensemble, as well as plasma effects, are not considered in this work.

The paper is structured as follows: in Sec. II we provide an outline of the four methods used to calculate the laser-induced fusion cross-section enhancements. Section III provides the subsequent results and Sec. IV provides conclusions and an outlook.

---

[*] john.bekx@marvelfusion.com

II. THEORY

The fusion reactions that will be considered in this paper are deuterium-tritium fusion, deuterium-helium fusion, and proton-boron fusion:

$$\mathrm{D} + \mathrm{T} \rightarrow {}^4_2\mathrm{He} + {}^1_0 n + 17.6\ \mathrm{MeV}, \tag{1}$$

$$\mathrm{D} + {}^3_2\mathrm{He} \rightarrow {}^4_2\mathrm{He} + {}^1_1 p + 18.3\ \mathrm{MeV}, \tag{2}$$

$${}^1_1 p + {}^{11}_5\mathrm{B} \rightarrow 3\,{}^4_2\mathrm{He} + 8.7\ \mathrm{MeV}. \tag{3}$$

The fusion cross section is modeled by the conventional form [22,25,26] as a function of the center-of-mass (CoM) energy $\mathcal{E}$:

$$\sigma(\mathcal{E}) = \frac{S(\mathcal{E})}{\mathcal{E}}\mathcal{T}, \tag{4}$$

which encapsulates the three processes that make up a fusion reaction: the initial collision described by the geometrical cross section $1/\mathcal{E}$, the quantum-mechanical tunneling described by the transparency $\mathcal{T}$, and finally the actual fusing of particles described by the astrophysical S factor $S(\mathcal{E})$. How these quantities are obtained is elaborated on in the following sections.

The two colliding nuclei are described by an effective one-dimensional time-dependent Schrödinger equation (TDSE) in terms of relative coordinates and given in the dipole approximation, which is inherently assumed by all methods used in this work. The dipole approximation is valid so long as the wavelength of the laser field is much larger than the spatial extent of the fusing system. For a further elaboration, we refer to Refs. [4,6,27].

A. Tunneling transparency

Semiclassical methods. For the SC methods, we use the methodology as laid out in our previous work [4] and provide only a concise overview of relevant formulas here. In the semiclassical approximation, the transparency can be calculated via

$$\mathcal{T} = e^{-2\mathrm{Im}\mathcal{S}/\hbar}, \tag{5}$$

where

$$\mathcal{S} = \begin{cases} \pm \int_{\text{tunnel}} dr p(r), & \text{for WKB} \\ \int_{\text{tunnel}} dt[L + \mathcal{E}], & \text{for ITM,} \end{cases} \tag{6}$$

and is valid so long as $\mathrm{Im}\mathcal{S} \gg \hbar$. In the WKB method, the imaginary part is obtained through

$$p(r) = \sqrt{2\mu[\mathcal{E} - V(r)]} = i\sqrt{2\mu[V(r) - \mathcal{E}]}, \tag{7}$$

where μ is the reduced mass and the choice in the sign of $\mathrm{Im}\mathcal{S}$ is taken to ensure an exponentially decaying behavior in the transparency. For the ITM, L is the conventional Lagrangian, $L = \mu\dot{r}(t)^2/2 - V(r(t))$, and the integration is taken over the time it takes to tunnel through the barrier along the subbarrier trajectory that satisfies the classical equations of motion. The imaginary part is obtained after making the change of coordinate $t = -i\tau$. For both of these methods, the potential is given by

$$V(r,t) = \frac{\kappa}{r} - eZ_{\mathrm{eff}}|\mathbf{E}|r\cos\theta\cos(\omega t + \varphi), \tag{8}$$

where $\kappa = e^2 Z_1 Z_2/4\pi\varepsilon_0$, with Z_1 and Z_2 the charge numbers of the reactants. The effective charge number is given by $Z_{\mathrm{eff}} = (Z_1 A_2 - Z_2 A_1)/(A_1 + A_2)$, with A_1 and A_2 the number of nucleons. The electric-field amplitude is denoted by $|\mathbf{E}|$ and the angle between the relative particle motion and the polarization direction is given by $\theta \in [0, \pi]$. Finally, ω refers to the angular photon frequency and φ denotes the phase of the electric field. For the inherently time-independent WKB method, $V(r) = V(r, t = 0)$. This potential only accounts for $r \in [R, \infty)$, where R denotes the length scale below which the strong nuclear force dominates over the Coulomb potential and is taken to be $R = 1.44(A_1^{1/3} + A_2^{1/3})$ fm [22]. Below this value, we assume a constant, flat nuclear potential well. For both methods, the integration is taken between the inner and outer classical turning points. The inner turning point is given by $R_{\mathrm{in}} = R$ (equal to 3.891 fm for DT and DHe^3 and 4.643 fm for $p\mathrm{B}^{11}$) and the outer one can be obtained from Eq. (8) using the relation $V(R_{\mathrm{out}}, 0) = \mathcal{E}$.

In our previous work [4], we found that the use of the SC methods is only applicable for a limited region of phase space, comprised of the laser parameters and the CoM energy, in the cases of DT and DHe^3 fusion. For this reason, we employ the Kramers-Henneberger (KH) method [23] in the dynamic-field case. The consideration of the SC methods was kept for benchmarking and studying $p\mathrm{B}^{11}$ fusion in the static case, which was not considered in our previous work.

Kramers-Henneberger method. For this part, we closely follow the derivation presented in Ref. [6]. The KH method consists of the following steps: a unitary transformation is made to the reference frame of an oscillating charged particle in an external electric field. In this new reference frame, the one-body wave function obeys a conventional one-body TDSE with a potential $V_{\mathrm{KH}}(\mathbf{r}, t) = \kappa/|\mathbf{r} - \mathbf{r}_e(t)|$, where $\mathbf{r}_e(t) = r_e\cos(\omega t)\hat{\mathbf{e}}_E$ and $r_e = eZ_{\mathrm{eff}}|\mathbf{E}|/(\mu\omega^2)$. Note that the direction and time dependence of $\mathbf{r}_e(t)$ are the same as those of the electric field $\mathbf{E}$. In the original paper of Henneberger [23], this potential is written out as an infinite sum over Bessel functions in a Floquet-like manner by using the Jacobi-Anger identity. Subsequently, the zeroth-order mode is shown to be time independent and in fact corresponds to an average over a single oscillation period. The remaining time-dependent terms may then be treated as a perturbative series. In practice, it is common to restrict oneself to the averaged (zeroth-order) form, which is a valid approximation so long as the temporal scale of the field is much faster than that of the process under consideration. After expanding $V_{\mathrm{KH}}(\mathbf{r}, t)$ in terms of Legendre polynomials, one arrives at

$$V_{\mathrm{KH}}(\mathbf{r}, t) = \frac{\kappa}{|\mathbf{r} - r_e\sin(\omega t)\hat{\mathbf{e}}_E|} = \kappa\sum_{l=0}^{\infty} P_l(\cos\theta) \times \begin{cases} \frac{r^l}{r_e^{l+1}}\frac{1}{|\sin(\omega t)|\sin^l(\omega t)}, & \text{for } r \leqslant |r_e\sin(\omega t)| \\ \frac{r_e^l\sin^l(\omega t)}{r^{l+1}}, & \text{for } r > |r_e\sin(\omega t)|. \end{cases} \tag{9}$$

For the averaging, we wish to calculate

$$V_{\mathrm{KH}}^{(0)}(\mathbf{r}) = \frac{1}{2\pi}\int_0^{2\pi} d\xi V_{\mathrm{KH}}(\mathbf{r},\xi), \tag{10}$$

with $\xi = \omega t$. Care must be taken when performing the integration to ensure the correct integrand from Eq. (9) is used as ξ goes over the unit circle. By exploiting some symmetries of the sine function, the expression for $V_{\mathrm{KH}}^{(0)}(\mathbf{r})$ can be brought in the following form:

$$V_{\mathrm{KH}}^{(0)}(\mathbf{r}) = \frac{2\kappa}{\pi}\sum_{l\in 2\mathbb{N}_0} P_l(\cos\theta) \times \left[\frac{r_e^l}{r^{l+1}}\int_0^\beta d\xi \sin^l\xi + \frac{r^l}{r_e^{l+1}}\int_\beta^{\pi/2}\frac{d\xi}{|\sin\xi|\sin^l\xi}\right], \tag{11}$$

where $\beta = \arcsin(r/r_e) \in [0,\pi/2)$. The analytical solution to these integrations is given by [6]

$$V_{\mathrm{KH}}^{(0)}(\mathbf{r}) = \frac{\kappa}{\pi r_e}\sum_{l\in 2\mathbb{N}_0} P_l(\cos\theta)\frac{\Gamma\left(\frac{l+1}{2}\right)}{\Gamma\left(\frac{l}{2}+1\right)} \times \left[A_l\left(\frac{r}{r_e}\right)^{-l-1} + B_l\left(\frac{r}{r_e}\right)^l\right], \tag{12}$$

where

$$A_l = \frac{2\beta}{\sqrt{\pi}} - \sum_{i=0}^{l/2}\frac{\Gamma(i)}{\Gamma\left(i+\frac{1}{2}\right)}\left(\frac{r}{r_e}\right)^{2i-1}\sqrt{1-\left(\frac{r}{r_e}\right)^2},$$
$$B_l = \sum_{i=0}^{l/2}\frac{\Gamma(i)}{\Gamma\left(i+\frac{1}{2}\right)}\left(\frac{r}{r_e}\right)^{-2i}\sqrt{1-\left(\frac{r}{r_e}\right)^2} - \frac{2\ln(\tan(\beta/2))}{\sqrt{\pi}}. \tag{13}$$

When $r > r_e$ for all values of ξ the result becomes more concise:

$$V_{\mathrm{KH}}^{(0)}(\mathbf{r}) = \frac{\kappa}{\sqrt{\pi}}\sum_{l\in 2\mathbb{N}_0} P_l(\cos\theta)\frac{r_e^l}{r^{l+1}}\frac{\Gamma\left(\frac{l+1}{2}\right)}{\Gamma\left(\frac{l}{2}+1\right)}. \tag{14}$$

To proceed, this potential is used in the WKB-transparency expression

$$\mathcal{T} = \exp\left\{-\frac{2}{\hbar}\int_{R_{\mathrm{in}}}^{R_{\mathrm{out}}} dr\sqrt{2\mu\left[V_{\mathrm{KH}}^{(0)}(\mathbf{r}) - \mathcal{E}\right]}\right\}. \tag{15}$$

The outer turning point is obtained numerically from the relation $V_{\mathrm{KH}}^{(0)}(R_{\mathrm{out}}) = \mathcal{E}$. The inner turning point comes from the largest vector in the collection of vectors that defines the interior, nuclear region: $\{\mathbf{r} \text{ for } |\mathbf{r} - \mathbf{r}_e(t)| \leqslant R, \forall\, t \in [0, 2\pi/\omega)\}$. It is the solution R_{in} of

$$\sqrt{R_{\mathrm{in}}^2 + r_e^2\sin^2\xi^* - 2R_{\mathrm{in}}r_e\cos\theta|\sin\xi^*|} = R, \tag{16}$$

where ξ^* maximizes the norm $|\mathbf{r} - \mathbf{r}_e(\xi^*)|$. In doing so, one arrives at

$$R_{\mathrm{in}} = \begin{cases} R + r_e, \text{ for } \theta = \pi\mathbb{Z} \\ R/\sin\theta, \text{ otherwise.}\end{cases} \tag{17}$$

Practically, one considers the minimum of these two values.

As to the applicability of the KH method, it was mentioned that the averaging is valid so long as the temporal scale of the laser is much faster than that of the fusion process. We follow the reasoning of Lv *et al.* [6] that, of the three processes that constitute a fusion reaction (collision, tunneling, and fusing), the collision is by far the slowest process, on a timescale of the order of femtoseconds. The corresponding restriction on the photon energies for which the KH method is valid is $\hbar\omega \geqslant 1$ keV.

The physical justification for the CNILE trend was addressed in Sec. III A of Ref. [4], which we repeat here for completeness. (This line of reasoning is based on the deformation interpretation of the laser-induced fusion enhancement.) The origin lies with the long tail of the field-free Coulomb potential between the reactants. Considering the same $\mathcal{E}$ for two pairs of fusion fuels, A and B, where one has a larger product of charge numbers than the other, say $\prod Z_A > \prod Z_B$, then the outer classical turning point of pair A lies further than that of pair B. Hence, the higher Coulombic repulsion for pair A results in a smaller transparency, as is intuitively clear. However, the deformation to this potential from the electric field is most prevalent for higher values of r, in the tail of the potential. Hence, the reduction of the outer turning point is more pronounced for pair A than for pair B, leading to an increased laser-induced enhancement for those fuel reactants with a larger Coulombic repulsion. This trend is also expected to be present in the transformed KH potential for the same reason.

In the VSA, the method relies on an energy averaging being taken, as will be shown below. However, since the prefactor $S(\mathcal{E})/\mathcal{E}$ in Eq. (4) is also dependent on the energy, it is less sensible to treat the transparency in the VSA separately. For this reason, we elaborate on this method in its own section below, complete with its own justification for expecting to observe the CNILE trend using the energy-gain interpretation. First, however, we quickly discuss the astrophysical S factor.

B. Astrophysical *S* factor

The astrophysical S factor is obtained by semi-empirical means. As was done in Ref. [4], the astrophysical S factor for DT and DHe^3 fusion used throughout this work was obtained from the work of Bosch and Hale [28] and provides a parametrized form for $S(\mathcal{E})$, which is valid for CoM energies in the ranges of [0.5, 550] keV and [0.3, 900] keV for DT and DHe^3, respectively. For pB^{11} fusion we employed the parametrization from Nevins and Swain [29]. In our previous work [4], we argued that the S factor employed must be corrected to account for the fact that we model the tunneling to a nonzero value of the nuclear well, whereas the parametrization of the S factor is obtained from an expression that inherently assumes $R = 0$. The correction was found to be

$$S_R(\mathcal{E}) = S_0(\mathcal{E})e^{\sqrt{\tilde{\mathcal{E}}_G(R)/\mathcal{E}} - \sqrt{\mathcal{E}_G/\mathcal{E}}}, \tag{18}$$

where $S_R(\mathcal{E})$ is the value to be used in Eq. (4), $S_0(\mathcal{E})$ is the semi-empirical value obtained from Refs. [28,29], and

$$\tilde{\mathcal{E}}_G(R) = \frac{4\mathcal{E}_G}{\pi^2}[\cos^{-1}(\sqrt{\rho}) - \sqrt{\rho(1-\rho)}]^2, \tag{19}$$

with $\mathcal{E}_G = 2\mu\kappa^2\pi^2/\hbar^2$ denoting the Gamow energy and $\rho = \mathcal{E}R/\kappa$. This correction also makes sense within the KH framework for the following reason: Although the consideration of a static field is not possible within the KH approximation because of the inherent high-frequency assumption, one may still revert to a field-free scenario by considering the limit $|\mathbf{E}| \to 0$. In that case, the KH method essentially boils down to the WKB method, but with tunneling to a nonzero R, as evinced by the transparency in Eq. (15) and the presence of R in Eq. (16), which warranted the use of the corrected S_R factor. In addition, for all methods considered, we assume that there is no discernible effect of the laser on the astrophysical S factor. (The validity of this assumption was addressed in Ref. [11].) Therefore, the use of the corrected S_R factor remains consistent within the KH framework as we return to finite values of $(|\mathbf{E}|, \omega)$.

C. Volkoff-state approximation

The full theoretical framework behind the VSA is outlined in the works of Wang [7] and Liu *et al.* [9], so we provide only a small recap of the relevant formulas.

In the absence of an external field, the wave function in CoM coordinates takes on the asymptotic form of a plane wave $\psi(\mathbf{r}, t) \sim \exp\{i(\mathbf{p}\cdot\mathbf{r} - \mathcal{E}t)/\hbar\}$, with $p = \sqrt{2\mu\mathcal{E}}$. When considering an external laser field, the asymptotic wave function gets an extra phase factor and is called a Volkoff state [24]:

$$\psi_V(\mathbf{r}, t) \sim \exp\left\{\frac{i}{\hbar}\left[\mathbf{p}\cdot\mathbf{r} - \mathcal{E}t - \int_0^t dt' H_I(t')\right]\right\}, \tag{20}$$

where the interaction Hamiltonian is given in the velocity gauge (the use of the Coulomb gauge is implied):

$$H_I(t) = -\frac{eZ_{\text{eff}}}{\mu}\mathbf{p}\cdot\mathbf{A}(t) + \frac{e^2 Z_{\text{eff}}^2}{2\mu}A^2(t). \tag{21}$$

The time dependence of the vector potential is subsequently assumed to be harmonic, which allows for a Fourier expansion of the Volkoff wave function and an analytical expression for the Volkoff phase. The harmonic time dependence also allows for us to make use of the simple relation $|\mathbf{E}| = A_0\omega$, with A_0 being the amplitude of the vector potential. The result of the Fourier expansion is

$$\mathcal{F}[\psi_V(\mathbf{r}, t)] = e^{i\mathbf{p}\cdot\mathbf{r}/\hbar} e^{iu} \sum_{n\in\mathbb{Z}} F_n(u, v) e^{-i(\mathcal{E}+U_p+n\hbar\omega)t/\hbar}, \tag{22}$$

$$F_n(u, v) = \frac{1}{2\pi}\int_0^{2\pi} d\xi\, e^{-iu\cos\xi + iv\sin 2\xi + in\xi}, \tag{23}$$

where u and v are dimensionless quantities given by $u = eZ_{\text{eff}}|\mathbf{E}|p\cos\theta/(\mu\hbar\omega^2)$ and $v = (eZ_{\text{eff}}|\mathbf{E}|)^2/(8\mu\hbar\omega^3)$. The ponderomotive energy $U_p = (eZ_{\text{eff}}|\mathbf{E}|)^2/(4\mu\omega^2)$ is the average quiver energy added to the effective particle of charge eZ_{eff} and is a strong-field effect that originates from the A^2 term. Note that Eqs. (22) and (23) reveal that there is a probability $P_n = |F_n(u, v)|^2$ (normalized to $\sum_{n\in\mathbb{Z}} P_n = 1$) of finding the particle in a state with an associated energy $\mathcal{E}_n \equiv \mathcal{E} + U_p + n\hbar\omega$. Positive and negative values of n denote the possible absorption and emission of n photons, respectively. Subsequently, a laser-enhanced cross section can be obtained by averaging the field-free cross section over all possible values of $\mathcal{E}_n$ using P_n as a probability function:

$$\sigma(\mathcal{E}, |\mathbf{E}|, \theta, \omega) = \sum_{n\in\mathbb{Z}} P_n(u, v)\sigma(\mathcal{E} + U_p + n\hbar\omega), \tag{24}$$

where the field-free cross section is given by $\sigma(\mathcal{E}) = [S_0(\mathcal{E})/\mathcal{E}]\exp(-\sqrt{\mathcal{E}_G/\mathcal{E}})$. We note that the use of the corrected astrophysical S factor $S_R(\mathcal{E})$ was not necessary because it is constructed explicitly to ensure that the expressions

$$\sigma(\mathcal{E}) = \frac{S_0(\mathcal{E})}{\mathcal{E}}e^{-\sqrt{\mathcal{E}_G/\mathcal{E}}} = \frac{S_R(\mathcal{E})}{\mathcal{E}}e^{-\sqrt{\tilde{\mathcal{E}}_G(R)/\mathcal{E}}}, \tag{25}$$

with $\tilde{\mathcal{E}}_G(R)$ given in Eq. (19), result in the same field-free cross section.

The sum over integers n is practically handled by cutoff values, for which analytical forms are given in Ref. [7]:

$$n_{\text{min}} = \begin{cases} -|u| + 2v, & \text{if } |u|/(8v) > 1 \\ -u^2/(16v) - 2v, & \text{if } |u|/(8v) \leqslant 1, \end{cases} \tag{26}$$

and $n_{\text{max}} = |u| + 2v$. However, it was stated that these expressions are valid only when n is large, consistent with the consideration of very low values of ω in Ref. [7] (higher values of n_{min} and n_{max} are associated with higher values of u and v, which are in turn larger for smaller values of ω). This large-n assumption is, however, not a guarantee for the parameters that will be considered in this work. So instead, we increased the values of n_{min} and n_{max} independently until the resulting value of $\sigma(\mathcal{E}, |\mathbf{E}|, \theta, \omega)$ converged. The values of n_{min} and n_{max} obtained in this way were found to be in close proximity to the values obtained with the analytical expressions mentioned above, although the latter ones typically missed the contributions from a few values of n. For this reason, the analytical expressions for n_{min} and n_{max} were not used for the calculation of results in this work. These expressions are still mentioned however, because they reveal how the limits on n depend on the external laser parameters. These dependencies remain unchanged for the limits obtained with our convergence approach, since they were found never to deviate far from the limits obtained analytically. In this way, we may also justify why we can expect to observe the CNILE trend with the VSA method. The reason lies with the dependence of U_p, u, and v on Z_{eff}. A larger Z_{eff} leads to a larger ponderomotive energy U_p leading to a larger overall enhancement, whereas larger values of u and v lead to a further contribution from absorbed photons.

As to the applicability of the VSA, the use of the separation coordinates again implies the use of the dipole approximation, which is attested to by the fact that the vector potential (and the consequent electric field) is assumed to be spatially uniform. The work of Wang [7] uses the amplitude of the quiver motion, $r_e = eZ_{\text{eff}}|\mathbf{E}|/(\mu\omega^2)$, to characterize the spatial extent of the fusing system. This must be much smaller than the spatial extent of the laser field. The largest quiver motion for all systems and parameters considered in this work was for $p\text{B}^{11}$ fusion at $|\mathbf{E}| = 10^{17}$ V/m and $\hbar\omega = 1$ keV, with a value of ≈5000 fm. The shortest laser wavelength considered, associated with $\hbar\omega = 10$ keV, is of the order of 125 000 fm,

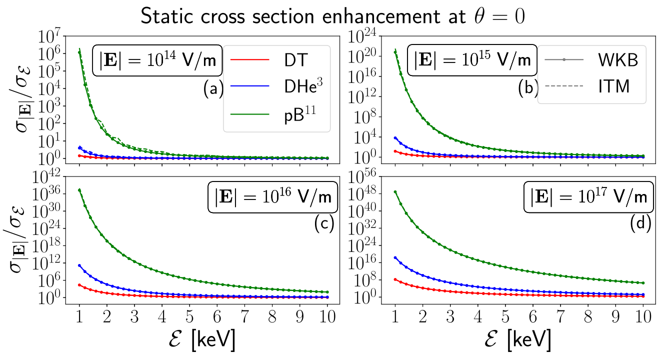

FIG. 1. The static-field cross section ($\sigma_{|\mathbf{E}|}$) divided by the field-free one ($\sigma_{\mathcal{E}}$) of DT (red), DHe^3 (blue), and pB^{11} (green) fusion at $\theta = 0$. For the grayscale version: blue, red, and green correspond respectively to hues of gray going from darker to lighter. The circle and dashed lines correspond to the WKB and ITM result, respectively. It can be seen that the trend observed in Ref. [4] persists for pB^{11}, which showcases the largest relative enhancement to the cross section for all electric-field strengths (a)–(d) $|\mathbf{E}| = 10^{14}$–10^{17} V/m considered, followed by DHe^3 and DT. In terms of absolute values however, the static DT cross section is still larger than the static DHe^3 cross section, which in turn is larger than the pB^{11} one for all parameters considered.

thus validating the use of the VSA for all considered systems and parameters.

III. RESULTS

In this section we show the results for the laser-enhanced fusion cross sections using the aforementioned methods. As an important first step, we illustrate that the SC methods continue to show that the CNILE trend persists for pB^{11} in the static-field case. This is shown in Fig. 1, where we plot the static-field cross section ($\sigma_{|\mathbf{E}|}$) relative to the field-free one ($\sigma_{\mathcal{E}}$) of DT (red; see figure captions for grayscale version), DHe^3 (blue), and pB^{11} (green) fusion as a function of the CoM energy $\mathcal{E}$ at $\theta = 0$. This particular polarization angle was chosen in favor of an angle-averaged result to circumvent the issue that may arise when $\cos\theta < 0$ in the employed dipole approximation resulting in a nonexistent classical turning point at the considered value of $\mathcal{E}$ (see Sec. II B of Ref. [4]). Each subplot in Fig. 1 denotes a different electric-field strength ranging from $|\mathbf{E}| = 10^{14}$ V/m to $|\mathbf{E}| = 10^{17}$ V/m. We note that, although the enhancement to the fusion cross section of pB^{11} may be seen to be quite exceptional, especially for lower values of $\mathcal{E}$, we emphasize that Fig. 1 shows a *relative* enhancement only. For all parameters considered in Fig. 1, the DT cross section still surpasses that of DHe^3 followed by the one of pB^{11} for all CoM energies shown. Interestingly however, the laser-enhanced pB^{11} fusion cross section does surpass the *field-free* one of DHe^3 for $|\mathbf{E}| = 10^{16}$ V/m (if $\mathcal{E} < 1.5$ keV) and for $|\mathbf{E}| = 10^{17}$ V/m (if $\mathcal{E} < 4$ keV). As to the validity of the SC methods in the static case, we mention that the lowest value of Im$\mathcal{S}$ used for the results in Fig. 1 is $4\hbar$, $8\hbar$, and $14\hbar$, for DT, DHe^3, and pB^{11}, respectively.

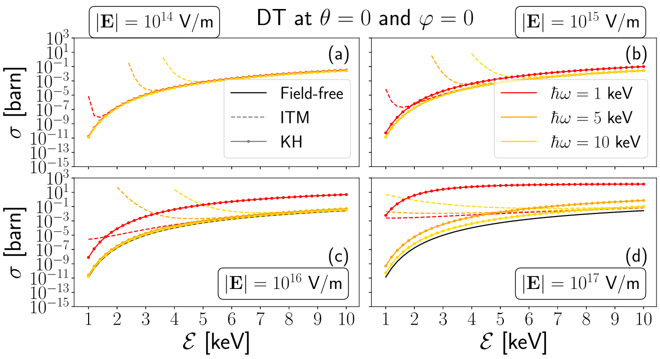

FIG. 2. The dynamic-field cross section of DT at $\theta = 0$ and $\varphi = 0$. The different subplots denote different electric-field strengths ranging over (a)–(d) $|\mathbf{E}| = 10^{14}$–10^{17} V/m, whereas the different photon energies are denoted in red ($\hbar\omega = 1$ keV), orange ($\hbar\omega = 5$ keV), and yellow ($\hbar\omega = 10$ keV). For the grayscale version: red, orange, and yellow correspond respectively to hues of gray going from darker to lighter. Finally, the dashed and circle lines refer to the ITM and KH result, respectively.

A. Semiclassical compared with Kramers-Henneberger

We proceed by considering a dynamic electric field. We first show a comparison of the dynamic-field cross section for DT fusion at $\theta = 0$ and $\varphi = 0$ between the ITM and the KH approximation, so as to highlight the differences between the predictions of both methods. This is illustrated in Fig. 2. Note that the KH result cannot distinguish between different values of the phase parameter φ due to the averaging over an oscillation period that is inherent to the method. There are several interesting observations to be made from Fig. 2.

First and foremost, we draw attention to the ITM results. The increased cross section for decreasing CoM energies, which was discussed in detail in Ref. [4] illustrates the breakdown of the SC method. Values that corresponded to Im$\mathcal{S} < \hbar$ have been omitted, but the sharply increased cross section is associated with transparency calculations where Im$\mathcal{S} \approx \hbar$ and the semiclassical approximation begins to break down.

Second, we compare the ITM results to the KH ones. Figure 2 illustrates that, not only do the ITM and KH results differ in a quantitative way, but more disconcertingly, they also differ qualitatively. Starting with the behavior the cross section exhibits as a function of the CoM energy $\mathcal{E}$ using the ITM, we can see that the enhancement is largest for smaller values of $\mathcal{E}$ and that for larger $\mathcal{E}$ values the cross section approaches the field-free one. Of course, this is ignoring the unphysical increasing cross section at lower $\mathcal{E}$ values, but this trend is also observed in the static case (Fig. 1), where no such unphysical behavior is seen. As was mentioned in Ref. [4], this trend was also predicted in the works of Wang [7] and Liu *et al.* [9]. Conversely, the KH results appear to predict a nearly constant enhancement to the cross section for all values of $\mathcal{E}$ considered. This is made most apparent by the results at $\hbar\omega = 1$ keV shown by the red circle lines. Only at $|\mathbf{E}| = 10^{17}$ V/m and $\hbar\omega = 1$ keV may it be argued that the low-$\mathcal{E}$ KH enhancement is larger than the high-$\mathcal{E}$ one. However, this appears to be more of a consequence from the fact that the dynamically enhanced cross section plateaus for these laser parameters. The KH result still predicts large enhancements for high $\mathcal{E}$ values, where the ITM predicts no enhancement whatsoever. For lower values of the electric-field strength ($|\mathbf{E}| = 10^{14}$ V/m), we may observe ranges of $\mathcal{E}$ where the two methods do agree with one another insofar as they show barely any enhancement at these laser parameters.

Next, we may focus our attention to the behavior of the cross section as the photon energy is increased. To put it concisely, both methods predict completely opposite trends. Whereas the ITM attributes larger enhancements to higher photon energies, in agreement with the work of Queisser and Schützhold [5], the KH method favors lower photon energies to this end, similar to the conclusions in works of Wang [7], Liu *et al.* [9], and Lv *et al.* [6,10,12].

Lastly, we note that the SC method and the KH method have already been previously compared with one another in the work by Liu *et al.* [9]. There, the behavior of the cross section with respect to an increased electric-field strength was focused on [see their Figs. 5(c) and 5(d)]. Their conclusion was the same as the one we are able to draw from Fig. 2, namely, that a larger value of $|\mathbf{E}|$ (in their work the intensity, $I = c\varepsilon_0|\mathbf{E}|^2/2$, was considered) results in a larger enhancement. The large discrepancies between the SC and KH method were not identified in Ref. [9], because only one value of $\mathcal{E}$ was considered, and only two values of $\hbar\omega$, one of which was $\hbar\omega = 1$ eV, being far below the value for applicability of the KH method. The discussion surrounding Fig. 2 was presented for the reason that the large quantitative and qualitative differences between the SC and KH predictions had not been discussed in preceding literature in the context of fusion processes.

Despite the large differences in predictions between the SC and KH results, they do both agree with regards to their prediction of the CNILE trend. The emergence of CNILE within the KH framework is shown in Fig. 3. Figure 3 shows the polarization-averaged fusion cross section, given by

$$\sigma_{\text{ave}}(\mathcal{E}, |\mathbf{E}|, \omega) = \frac{1}{2}\int_0^{\pi} d\theta\, \sigma(\mathcal{E}, |\mathbf{E}|, \theta, \omega) \sin\theta, \qquad (27)$$

of DT (red), DHe^3 (blue), and pB^{11} (green) fusion. The different subplots again denote the range of electric-field strengths $|\mathbf{E}| = 10^{14}$–10^{17} V/m and the photon energies of $\hbar\omega = 1$, 5, 10 keV are given by the solid, dashed, and dotted lines, respectively. The field-free cross sections for the three fusion fuels are also denoted with solid black lines.

We can conclude that the KH method predicts no enhancement to the fusion cross section before a critical value of the electric-field strength is reached, similar to the conclusion of the SC method in the static case [4,5,9]. In addition, it can be observed that lower values of the photon energy are favored in combination with high $|\mathbf{E}|$ values, in agreement with the work of Lv *et al.* [6], which provides merit for their use of the dimensionless parameter $n_d = eZ_{\text{eff}}|\mathbf{E}|/(\mu\omega^2 R) = r_e/R$. The enhancement they predict with increasing values of n_d are consistent both with increasing values of $|\mathbf{E}|$ and decreasing values of ω. We point out that an increased value of n_d, and subsequent enhancement, can also be associated with an increased value of $Z_{\text{eff}} = (Z_1A_2 - Z_2A_1)/(A_1 + A_2)$ and a reduction of μ. Therefore, increasing the number of charge neutral nucleons is expected to cause a transparency suppression, but increasing either Z_1 or Z_2, or both, results in a larger n_d, and therefore a larger enhancement. Thus, the CNILE trend is justifiably observed in Fig. 3, as expected. We may even conclude that for the extremely intense field at $|\mathbf{E}| = 10^{17}$ V/m, with the relatively low photon energy of $\hbar\omega = 1$ keV, the pB^{11} fusion cross section may surpass those of the *enhanced* cross sections of DT and DHe^3 fusion.

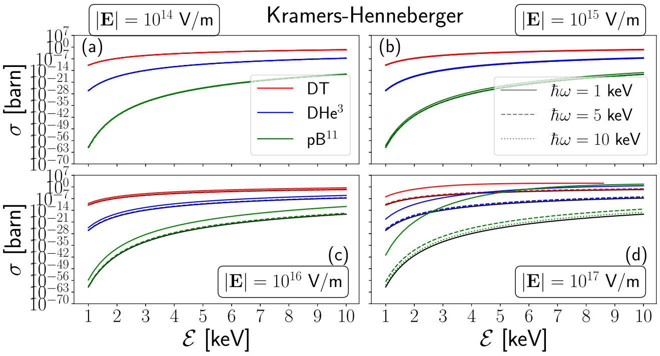

FIG. 3. The polarization-averaged dynamic-field cross section of DT (red), DHe^3 (blue), and pB^{11} (green) fusion. For the grayscale version: blue, red, and green correspond respectively to hues of gray going from darker to lighter. The different subplots denote different electric-field strengths ranging over (a)–(d) $|\mathbf{E}| = 10^{14}$–10^{17} V/m, whereas the different photon energies are denoted by the solid ($\hbar\omega =$ 1 keV), dashed ($\hbar\omega = 5$ keV), and dotted ($\hbar\omega = 10$ keV) lines. The field-free cross sections are depicted by the solid black lines. One can see that, for the extremely intense field at $|\mathbf{E}| = 10^{17}$ V/m, but with relatively low photon energy of $\hbar\omega = 1$ keV, the pB^{11} fusion cross section may surpass those of the *enhanced* cross sections of DT and DHe^3 fusion.

For completeness, we mention that Fig. 3 does not show values for the DT fusion cross section at $|\mathbf{E}| = 10^{17}$ V/m and $\hbar\omega = 1$ keV for $\mathcal{E} \geqslant 8.5$ keV. This is because at these values, the CoM energy surpasses the peak of the KH potential, for which a treatment using quantum tunneling is no longer consistent. Lastly, we mention that, for specific laser parameters, the KH potential may exhibit some unorthodox behavior that has previously not been commented on in the literature in the context of fusion reactions. The KH potential for pB^{11} at $|\mathbf{E}| = 10^{17}$ V/m, $\hbar\omega = 1$ keV, and $\theta = \pi/45$ is plotted as function of r in Fig. 4. The feature we wish to highlight is the emergence of a local maximum at $r \approx 600$ fm for DT and DHe^3 and at $r \approx 2100$ fm for pB^{11}. We found this emergence to be generally rare, requiring a combination of a large $|\mathbf{E}|$, a relatively low $\hbar\omega$ and a small $\theta > 0$. Nevertheless, a transparency calculation at a value of $\mathcal{E} \approx 7.5$ keV, $\approx$15 keV, and $\approx$11 keV for DT, DHe^3, and pB^{11}, respectively, will effectively involve an initial tunneling through the first bump, followed by a conventional propagation with a nontrivial potential and ending with a final tunneling through a second bump and into the nuclear well. Because of the rarity of this phenomenon, we have approximated the transparency in such cases as the product of the transparencies through each of the bumps. This effectively boils down to the assumption

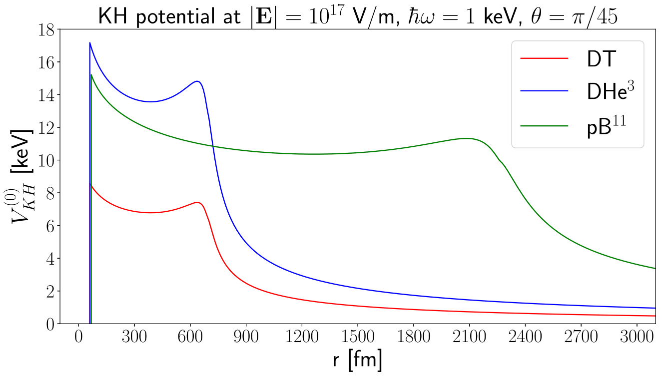

FIG. 4. The KH potential $V_{\mathrm{KH}}^{(0)}$ in keV as a function of r in fm at $|\mathbf{E}| = 10^{17}$ V/m, $\hbar\omega = 1$ keV, and $\theta = \pi/45$ of DT (red), DHe^3 (blue), and pB^{11} (green) fusion. For the grayscale version: blue, red, and green correspond respectively to hues of gray going from darker to lighter. The inner turning point lies at $R_{\mathrm{in}} = 55.78$ fm for DT and DHe^3 and at $R_{\mathrm{in}} = 66.55$ fm for pB^{11}. The bumps at $r = 600$ fm and $r = 2100$ fm are found to only be present for a combination of very large $|\mathbf{E}|$, relatively low $\hbar\omega$ and small $\theta > 0$. Transparency calculations at a $\mathcal{E}$ value that involves the bump are calculated as the product of the transparencies through the first and second bump.

that after the first tunneling, all of the wave packet of the fusing particles manages to propagate towards the second bump and initiate the second tunneling. We expect this to be a valid assumption seeing as a similar one has been employed for all prior calculations in both the SC and KH frameworks, in which cases the effect of the potential on the initial approach of the colliding particles was ignored.

Considering the breakdown of the SC methods for most of the relevant dynamic-laser parameters, we proceed by comparing the KH results with the VSA predictions and discuss their respective differences.

B. Kramers-Henneberger compared with Volkoff-state approximation

In Fig. 5, we compare the KH and VSA predictions of the dynamically enhanced fusion cross section of DT at $\theta = 0$ and $\varphi = 0$, similar to what was done in Fig. 2 for the comparison between the ITM and the KH method. Despite the clear quantitative differences, especially at $\hbar\omega = 1$ keV, one may observe that, contrary to the ITM, the VSA appears to illustrate some qualitative similarities with the KH results. As before, larger electric-field strengths result in larger enhancements, so long as a minimal critical value is reached ($|\mathbf{E}| \approx 10^{15}$–$10^{16}$ V/m), as is agreed on by all methods. The VSA results for DT agree with the trend observed with the KH method that a larger enhancement stems from smaller photon energies rather than large ones, for most values of the CoM energy $\mathcal{E}$. Conversely, the enhancement behavior of the VSA with respect to the CoM energy appears to match that of the SC methods, as we can see large enhancements for small $\mathcal{E}$ values, which begin to wane as $\mathcal{E}$ is increased. This is most notable for $|\mathbf{E}| = 10^{17}$ V/m, although a small rise at $|\mathbf{E}| = 10^{15}$ V/m can already be observed for low $\mathcal{E}$ and high $\hbar\omega$.

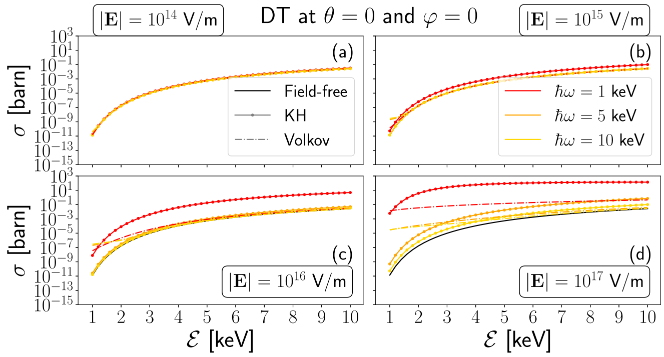

FIG. 5. The dynamic-field cross section of DT at $\theta = 0$ and $\varphi = 0$. The different subplots denote different electric-field strengths ranging over (a)–(d) $|\mathbf{E}| = 10^{14}$–10^{17} V/m, whereas the different photon energies are denoted in red ($\hbar\omega = 1$ keV), orange ($\hbar\omega = 5$ keV), and yellow ($\hbar\omega = 10$ keV). For the grayscale version: red, orange, and yellow correspond respectively to hues of gray going from darker to lighter. Finally, the circle and dash-dotted lines refer to the KH and VSA result, respectively.

The behavior of the dynamically enhanced cross section may be understood from the definition of $\mathcal{E}_n = \mathcal{E} + U_p + n\hbar\omega$ and the differences between $\sigma(\mathcal{E})$ and the relevant $\sigma(\mathcal{E}_n)$ in Eq. (24). For DT, and not considering $|\mathbf{E}| = 10^{17}$ V/m, the largest value for the ponderomotive energy occurs at $|\mathbf{E}| = 10^{16}$ V/m and $\hbar\omega = 1$ keV, with a value of $U_p = 34.6$ eV. For all CoM energies shown, the difference between $\sigma(\mathcal{E})$ and $\sigma(\mathcal{E} + 34.6\ \mathrm{eV})$ is not discernible on a log-scale. Thus, in Figs. 5(a)–5(c), the enhancement arises purely from the contribution of absorbed photons. The number of relevant photons is seen to rise for larger values of u and v from Eq. (26), and below, in the limit for large n. As u and v scale as ω^{-2} and ω^{-3}, respectively, this appears to indicate enhancement is favored for low photon energies. However, this is not true for all values of $\mathcal{E}$ as can be seen in Fig. 5 for $|\mathbf{E}| = 10^{16}$ V/m and low $\mathcal{E}$. Thus, the number n alone is not a general indicator for enhancement, because a single contribution $n = 1$ at $\hbar\omega = 10$ keV may outweigh the contributions of several values of n at a lower photon energy. The enhancement behavior may rather be explained through the interplay between $P_n(u, v)$ and $\sigma(\mathcal{E}_n)$. We consider $\mathcal{E} = 1$ keV at $|\mathbf{E}| = 10^{16}$ V/m and show in Table I the relevant values of $\sigma(\mathcal{E}_n)$ and $P_n(u, v)\sigma(\mathcal{E}_n)$, for $\hbar\omega = 1$ keV and $\hbar\omega = 10$ keV at $\theta = 0$. From Table I we may discern that at the lower photon energy of $\hbar\omega = 1$ keV, there are indeed contributions from more values of n than at $\hbar\omega = 10$ keV. However, the resulting values of $P_n(u, v)\sigma(\mathcal{E}_n)$ are dominated by the contributions from $n = 1$ and $n = 2$ at $\hbar\omega = 1$ keV. However, these are still below the dominant contribution of $P_n(u, v)\sigma(\mathcal{E}_n)$ at $n = 1$ for $\hbar\omega = 10$ keV, which results in the larger enhancement for the higher photon energy at these parameters. We note that the analytical expressions for n_{min} and n_{max} [Eq. (26) and below] state that only $n = 0$ would provide a contribution in both of these cases, which does not capture the small bumps observed at the low values of $\mathcal{E}$. Then again, it was already stated that these expressions were only valid in the limit for large n. If we consider higher values of $\mathcal{E}$, we may observe that the VSA predictions follow

TABLE I. Values of $\sigma(\mathcal{E}_n) = \sigma(\mathcal{E} + U_p + n\hbar\omega)$ and $P_n(u, v)\sigma(\mathcal{E}_n)$ for DT fusion at $\mathcal{E} = 1$ keV, $|\mathbf{E}| = 10^{16}$ V/m, and $\theta = 0$ at $\hbar\omega = 1$ keV (left) and $\hbar\omega = 10$ (right). Cross sections are given in barns.

	$\hbar\omega = 1$ keV		$\hbar\omega = 10$ keV	
n	$\sigma_n(\mathcal{E})$	$P_n(u, v)\sigma(\mathcal{E}_n)$	$\sigma_n(\mathcal{E})$	$P_n(u, v)\sigma(\mathcal{E}_n)$
-1	1.28×10^{-75}	8.42×10^{-77}	–	–
0	2.36×10^{-11}	2.05×10^{-11}	1.37×10^{-11}	1.37×10^{-11}
1	2.01×10^{-7}	1.27×10^{-8}	4.16×10^{-2}	2.88×10^{-7}
2	1.08×10^{-5}	1.90×10^{-8}	4.78×10^{-1}	7.012×10^{-11}
3	1.14×10^{-4}	3.07×10^{-9}	–	–
4	5.63×10^{-4}	1.55×10^{-10}	–	–

TABLE II. Values of $\sigma(\mathcal{E}_n) = \sigma(\mathcal{E} + U_p + n\hbar\omega)$ and $P_n(u, v)\sigma(\mathcal{E}_n)$ for pB^{11} fusion at $\mathcal{E} = 1$ keV, $|\mathbf{E}| = 10^{14}$ V/m, and $\theta = 0$ at $\hbar\omega = 1$ keV (left) and $\hbar\omega = 10$ (right). Cross sections are given in barns.

	$\hbar\omega = 1$ keV		$\hbar\omega = 10$ keV	
n	$\sigma_n(\mathcal{E})$	$P_n(u, v)\sigma(\mathcal{E}_n)$	$\sigma_n(\mathcal{E})$	$P_n(u, v)\sigma(\mathcal{E}_n)$
-1	–	–	–	–
0	1.06×10^{-60}	1.06×10^{-60}	1.05×10^{-60}	1.05×10^{-60}
1	6.94×10^{-42}	3.93×10^{-46}	3.80×10^{-16}	2.15×10^{-24}
2	1.37×10^{-33}	1.71×10^{-42}	5.52×10^{-11}	5.42×10^{-27}
3	1.15×10^{-28}	1.77×10^{-42}	–	–
4	2.56×10^{-25}	3.31×10^{-44}	–	–

the $\mathcal{E}$ trend of the SC methods, insofar as larger enhancements are predicted for lower values of $\mathcal{E}$, which stems from the fact that the field-free cross section plateaus. Hence, at higher values of $\mathcal{E}$, the differences between $\sigma(\mathcal{E}_0)$ and the relevant $\sigma(\mathcal{E}_n)$ diminish, which results in the observed convergence of the enhanced cross section results for $\hbar\omega = 1, 5, 10$ keV and $|\mathbf{E}| \leqslant 10^{16}$ V/m in Fig. 5.

Finally, the DT cross section for $|\mathbf{E}| = 10^{17}$ V/m at $\hbar\omega = 1$ keV dominates over those at other photon energies because the contribution from the ponderomotive energy at $\hbar\omega = 1$ keV, being $U_p = 3.46$ keV at these parameters, causes a large enhancement to the cross section for all CoM energies, explaining the behavior observed in Fig. 5(d).

The work of Wang [7] used the VSA method to show that large enhancements to the DT fusion cross section are favored by the lower photon energies. This may be true for the low values of $\hbar\omega$ that they considered (1.55–12.4 eV), but we already found that this is not true for all values of $\mathcal{E}$ and $\hbar\omega$, as was illustrated in Fig. 5. Moreover, we may show that this assessment is also not generally true for all fusion fuels, as is illustrated in Fig. 6. Figure 6 shows the exact same information as in Fig. 5, but for pB^{11} fusion rather than DT. The most striking feature that may be observed from Fig. 6 occurs for $|\mathbf{E}| < 10^{17}$ V/m and illustrates a reversal in the trend of the enhancement as a function of the photon energy. For $|\mathbf{E}| = 10^{14}$–10^{16} V/m and low values of $\mathcal{E}$, we can see that the higher enhancements are actually favored by the *higher* photon energies, in striking contrast with the predictions for DT in Fig. 5. If one considers $|\mathbf{E}| = 10^{16}$ V/m, the pB^{11} cross section of $\hbar\omega = 1$ keV overtakes those of the higher photon energies again for $\mathcal{E} \gtrapprox 7$ keV, and for $|\mathbf{E}| = 10^{17}$ V/m the trend has flipped back, again exhibiting the largest enhancement for the lowest photon energy.

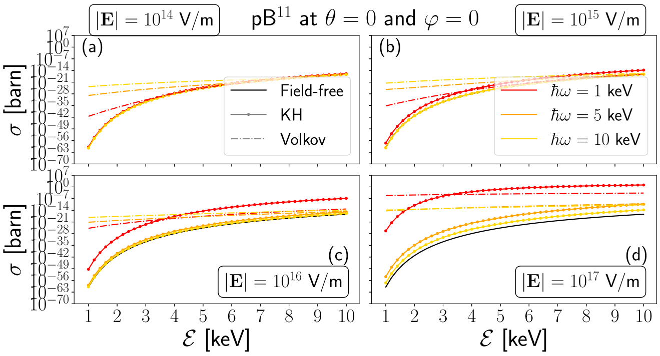

FIG. 6. The dynamic-field cross section of pB^{11} at $\theta = 0$ and $\varphi = 0$. The different subplots denote different electric-field strengths ranging over (a)–(d) $|\mathbf{E}| = 10^{14}$–10^{17} V/m, whereas the different photon energies are denoted in red ($\hbar\omega = 1$ keV), orange ($\hbar\omega = 5$ keV), and yellow ($\hbar\omega = 10$ keV). For the grayscale version: red, orange, and yellow correspond respectively to hues of gray going from darker to lighter. Finally, the circle and dash-dotted lines refer to the KH and VSA result, respectively.

The reason for this may again be explained by considering $P_n(u, v)\sigma(\mathcal{E}_n)$ and stems from the fact that the field-free cross sections for pB^{11} cross section may be incredibly small. Let us consider $\mathcal{E} = 1$ keV, $|\mathbf{E}| = 10^{14}$ V/m, and $\theta = 0$, for $\hbar\omega = 1$ keV and $\hbar\omega = 10$ keV. This low value for $|\mathbf{E}|$ is chosen because, at these values $U_p < 1$ eV, so the enhancement is again solely due to the photon absorption. We show the relevant values for $\sigma(\mathcal{E}_n)$ and $P_n(u, v)\sigma(\mathcal{E}_n)$ at these parameters in Table II. From Table II, we can see that the highest probability, P_n, comes from the contribution of $n = 0$. However, the cross section $\sigma(\mathcal{E}_0)$ may be so minute that, despite the low value of $P_n(u, v)$ at other values of n, their resulting contribution of $P_n(u, v)\sigma(\mathcal{E}_n)$ may still be the dominant factor. Consider, for example, the $n = 1$ contribution at $\hbar\omega = 10$ keV. Despite $P_1(u, v) \approx 10^{-8}$, it still provides the dominant contribution because the difference between $\sigma(\mathcal{E}_0)$ and $\sigma(\mathcal{E}_1)$ is so large. This difference is reduced for lower values of the photon energy, which results in a smaller enhancement. The trend flips back (enhancement favored by low $\hbar\omega$) for $|\mathbf{E}| = 10^{17}$ V/m, because the contribution from the ponderomotive energy dominates at $\hbar\omega = 1$ keV ($U_p = 28.3$ keV). These large differences, of many orders of magnitude, between $\sigma(\mathcal{E}_0)$ and $\sigma(\mathcal{E}_1)$ are not present in DT fusion for the photon energies that are being considered. Hence, this behavior did not appear for DT fusion.

Finally, we use the VSA method to compare the dynamically enhanced fusion cross section between the three fuels of DT, DHe^3, and pB^{11} fusion in Fig. 7. The CNILE trend is clearly seen to persist in the VSA framework. This makes sense, as a larger Z_{eff} leads to a larger ponderomotive energy U_p, potentially leading to a larger overall enhancement. In

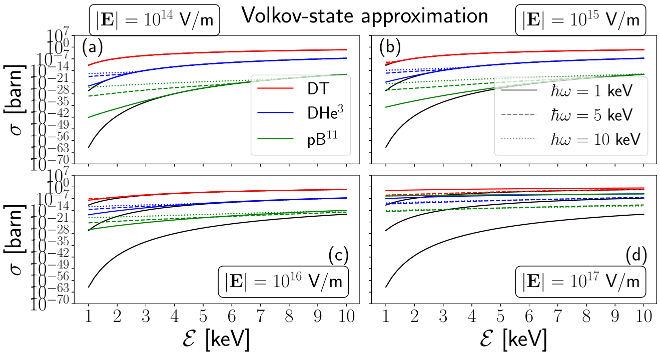

FIG. 7. The polarization-averaged dynamic-field cross section of DT (red), DHe^3 (blue), and pB^{11} (green) fusion. For the grayscale version: blue, red, and green correspond respectively to hues of gray going from darker to lighter. The different subplots denote different electric-field strengths ranging over (a)–(d) $|\mathbf{E}| = 10^{14}$–10^{17} V/m, whereas the different photon energies are denoted by the solid ($\hbar\omega = 1$ keV), dashed ($\hbar\omega = 5$ keV), and dotted ($\hbar\omega = 10$ keV) lines. The field-free cross sections are depicted by the solid black lines. One can see that, for the extremely intense field at $|\mathbf{E}| = 10^{17}$ V/m, but with relatively low photon energy of $\hbar\omega = 1$ keV, the pB^{11} fusion cross section may surpass that of the *enhanced* cross section DHe^3 fusion. However, the VSA predicts the enhanced pB^{11} fusion cross section remains just shy of the DT one for these parameters.

addition, a larger Z_{eff} leads to larger values of u and v, which in return result in more contributions from absorbed photons. One can see that the enhanced pB^{11} fusion cross section falls short of surpassing the enhanced cross section of DT at the extreme parameters $|\mathbf{E}| = 10^{17}$ V/m and $\hbar\omega = 1$ keV. However, it does coalesce with the enhanced DHe^3 cross section at these parameters. We also note that both the KH and the VSA results at $|\mathbf{E}| = 10^{17}$ V/m and $\hbar\omega = 1$ keV predict that the enhanced pB^{11} fusion cross section surpasses the field-free DT one, albeit for different regions of the CoM energy ($\mathcal{E} \gtrapprox 5$ keV for KH and $\mathcal{E} \lessapprox 2.5$ keV for VSA).

It remains to be discussed which of the two methods, the KH approximation or the VSA, provides the more realistic results for the dynamically enhanced fusion cross section. Both methods employ the dipole approximation and it was verified that this approximation is valid for all parameters considered in this work. We suspect the issue arises in the KH approximation, from the inherent approximation that the timescale of the laser field is much faster than the timescale of the fusion process. It was reasoned in the work of Lv *et al.* [6] that the fusion process is dominated by the timescale of the initial collision, occurring on the order of femtoseconds. The corresponding energy scale is $h/(1\text{ fs}) \approx 4$ eV. Subsequently, considering an energy scale for the laser field three orders of magnitude higher is a safe estimate, which is why Lv *et al.* postulated the KH approximation is valid for $\hbar\omega \geqslant 1$ keV (used throughout this work as well). However, the KH formalism specifically calculates the tunneling transparency and the initial collision plays no role in the calculation. Thus, the relevant timescale for the KH calculation is the tunneling time, which is of the order of attoseconds, or below, corresponding to an energy scale of 4 keV or higher. Thus, the energy scale of the laser field should be around 100 keV or higher for the KH approximation to be valid. For this reason, it seems likely the KH approximation is being applied in a regime where it should not. For validation, one could compare the KH and VSA results at very high values of $\hbar\omega$ (>100 keV) to determine whether they agree. However, at these high photon energies, the dipole approximation breaks down, so this verification could not be performed. Another note is the fact that the KH method uses the WKB expression for the transparency [Eq. (15)] and is therefore implicitly subjected to, at least in part, the assumptions made in the SC methods. For these reasons, we postulate the VSA method to be the most accurate one of all methods considered with regards to the qualitative predictions of laser-induced fusion enhancements.

IV. CONCLUSIONS AND OUTLOOK

In this paper, we sought to investigate the remark made in Ref. [4], which stated that the static-laser-induced enhancement to the fusion cross section is larger for fusion fuels that exhibit a higher Coulombic repulsion. To give it a name, we have dubbed this charge-number-increased laser-enhancement as CNILE.

After confirming the CNILE trend to persist in the static case for the considered fusion fuels of DT, DHe^3, and pB^{11} using the SC methods of the WKB approximation and the ITM, we considered whether this trend also emerged in the case of a dynamic external electric field. To compare with the ITM in the dynamic case, we have first employed the KH method. When comparing both methods, we found their predictions differed drastically, disagreeing both quantitatively and qualitatively. Whereas the ITM predicts larger cross-section enhancements for lower CoM energies and higher photon energies, the KH method is almost insensitive to the effect of changing the CoM energy and in addition favors smaller photon energies for larger enhancements. The origin for these discrepancies is rooted in the fact that the ITM is far outside of its realm of applicability for most laser parameters considered, as concluded by Ref. [4].

Subsequently, we used the KH method to calculate the dynamic fusion cross section enhancement for DT, DHe^3, and pB^{11}. We found the enhancement to be largest for pB^{11} for all parameters considered, thus confirming the existence of the CNILE trend in the dynamic case as well. The CNILE trend can be explained by considering the long potential tail of the Coulombic repulsion in the absence of an external field. A field-induced deformation to this potential is most drastic for larger separations. Thus, the largest increase in transparency is associated with the lowest field-free transparency, which is intuitively understandable to correspond to the largest Coulombic repulsion. In the case of an extremely intense field ($|\mathbf{E}| = 10^{17}$ V/m), but with a relatively low photon energy ($\hbar\omega = 1$ keV), we could conclude that the pB^{11} fusion cross section could surpass those of the *enhanced* cross sections of DT and DHe^3 fusion. Therefore, we predict the consideration of pB^{11} to be of vital importance in future laser-enhanced fusion experiments.

Finally, we compared the results of the KH method to those predicted using the VSA. Again, we found rather substantial differences between both methods. They both predict larger enhancements for high electric-field strengths, but the VSA matches the trend observed with the SC methods insofar as that larger enhancements are calculated for lower values of the CoM energy. More strikingly, the VSA results predicted no general trend for the enhancement behavior in terms of the photon energies. For DT, the larger enhancements were favored by lower photon energies for most CoM energies, whereas for $p\mathrm{B}^{11}$ fusion no general trend could be discerned. The discrepancy between both methods was argued to have arisen from the KH method being used outside of the realm where it can be considered valid. Nevertheless, the CNILE trend was again seen to persist within the VSA framework and could be attributed to the increased energy gain from the laser field to the fusing system as their respective charge numbers increased. Both the KH and the VSA method predicted the enhanced $p\mathrm{B}^{11}$ cross section could surpass the nonenhanced DT one at $|\mathbf{E}| = 10^{17}$ V/m and $\hbar\omega = 1$ keV.

As a final comment, it appears there is a peculiar trend shared by both the SC methods and the KH method, namely, that the larger cross-section enhancement is predicted if one moves towards the region of laser-parameter phase space where each of the respective methods start to break down. This makes it inherently difficult to make accurate predictions for optimal laser parameters to be used in an experiment. This, in combination with the large discrepancies between all methods considered warrants for transparency calculations using more sophisticated methods for benchmarking, such as the use of numerical solutions to the radial Schrödinger equation or time-dependent wave-packet propagation. Although this development is currently already underway, the lack of accurate models of the nuclear potential and the effects of the laser field on it, means this would simply result in yet another prediction framework, with no real data to compare it to. Therefore, we once more advocate for the absolute necessity of experiments in the field of laser-induced fusion enhancement.

ACKNOWLEDGMENTS

The authors would like to express their gratitude to Christian Bild for fruitful discussions. M.L.L. acknowledges support by the National Science Foundation under award PHY — 1903414.

[1] A. B. Zylstra, O. A. Hurricane, D. A. Callahan, A. L. Kritcher, J. E. Ralph, H. F. Robey, J. S. Ross, C. V. Young, K. L. Baker, D. T. Casey *et al.*, Burning plasma achieved in inertial fusion, Nature (London) **601**, 542 (2022).

[2] A. L. Kritcher, C. V. Young, H. F. Robey, C. R. Weber, A. B. Zylstra, O. A. Hurricane, D. A. Callahan, J. E. Ralph, J. S. Ross, K. L. Baker *et al.*, Design of inertial fusion implosions reaching the burning plasma regime, Nat. Phys. **18**, 251 (2022).

[3] E. Gibney, Nuclear-fusion reactor smashes energy record, Nature **602**, 371 (2022).

[4] J. J. Bekx, M. L. Lindsey, S. H. Glenzer, and K.-G. Schlesinger, Applicability of semiclassical methods for modeling laser-enhanced fusion rates in a realistic setting, Phys. Rev. C **105**, 054001 (2022).

[5] F. Queisser and R. Schützhold, Dynamically assisted nuclear fusion, Phys. Rev. C **100**, 041601(R) (2019).

[6] W. Lv, H. Duan, and J. Liu, Enhanced deuterium-tritium fusion cross sections in the presence of strong electromagnetic fields, Phys. Rev. C **100**, 064610 (2019).

[7] X. Wang, Substantially enhanced deuteron-triton fusion probabilities in intense low-frequency laser fields, Phys. Rev. C **102**, 011601(R) (2020).

[8] C. Kohlfürst, F. Queisser, and R. Schützhold, Dynamically assisted tunneling in the impulse regime, Phys. Rev. Res. **3**, 033153 (2021).

[9] S. Liu, H. Duan, D. Ye, and J. Liu, Deuterium-tritium fusion process in strong laser fields: Semiclassical simulation, Phys. Rev. C **104**, 044614 (2021).

[10] W. Lv, B. Wu, H. Duan, S. Liu, and J. Liu, Phase-dependent cross sections of deuteron-triton fusion in dichromatic intense fields with high-frequency limit, Eur. Phys. J. A **58**, 54 (2022).

[11] B. Wu, H. Duan, and J. Liu, Resonant tunneling of deuteron-triton fusion in strong high-frequency electromagnetic fields, Phys. Rev. C **105**, 064615 (2022).

[12] W. Lv, H. Duan, and J. Liu, Enhanced proton-boron nuclear fusion cross sections in intense high-frequency laser, Nucl. Phys. A **1025**, 122490 (2022).

[13] P. Emma, R. Akre, J. Arthur, R. Bionta, C. Bostedt, J. Bozek, A. Brachmann, P. Bucksbaum, R. Coffee, F.-J. Decker *et al.*, First lasing and operation of an ångstrom-wavelength free-electron laser, Nat. Photonics **4**, 641 (2010).

[14] T. Ishikawa, H. Aoyagi, T. Asaka, Y. Asano, N. Azumi, T. Bizen, H. Ego, K. Fukami, T. Fukui, Y. Furukawa *et al.*, A compact x-ray free-electron laser emitting in the sub-ångström region, Nat. Photonics **6**, 540 (2012).

[15] T. Tschentscher, C. Bressler, J. Grünert, A. Madsen, A. P. Mancuso, M. Meyer, A. Scherz, H. Sinn, and Ulf Zastrau, Photon beam transport and scientific instruments at the european XFEL, Appl. Sci. **7**, 592 (2017).

[16] W. Decking, S. Abeghyan, P. Abramian, A. Abramsky, A. Aguirre, C. Albrecht, P. Alou, M. Altarelli, P. Altmann, K. Amyan *et al.*, A MHz-repetition-rate hard x-ray free-electron laser driven by a superconducting linear accelerator, Nat. Photonics **14**, 391 (2020).

[17] H.-S. Kang, C.-K. Min, H. Heo, C. Kim, H. Yang, G. Kim, I. Nam, S. Y. Baek, H.-J. Choi, G. Mun *et al.*, Hard x-ray free-electron laser with femtosecond-scale timing jitter, Nat. Photonics **11**, 708 (2017).

[18] C. J. Milne, T. Schietinger, M. Aiba, A. Alarcon, J. Alex, A. Anghel, V. Arsov, C. Beard, P. Beaud, S. Bettoni *et al.*, SwissFEL: The swiss x-ray free electron laser, Appl. Sci. **7**, 720 (2017).

[19] D. J. Griffiths, *Introduction to Quantum Mechanics*, 2nd ed. (Pearson Education, Upper Saddle River, 2005).

[20] J. J. Sakurai, *Modern Quantum Mechanics*, 2nd ed. (Pearson Education, Upper Saddle River, 2011).

[21] V. S. Popov, Imaginary-time method in quantum mechanics and field theory, Phys. At. Nucl. **68**, 686 (2005).

[22] S. Atzeni and J. Meyer-ter-Vehn, *The Physics of Inertial Fusion: Beam Plasma Interaction, Hydrodynamics, Hot Dense Matter* (Oxford University Press, Oxford, 2004).

[23] W. C. Henneberger, Perturbation Method for Atoms in Intense Light Beams, Phys. Rev. Lett. **21**, 838 (1968).

[24] D. M. Volkov, Über eine klasse von Lösungen der Diracschen Gleichung, Eur. Phys. J. A **94**, 250 (1935).

[25] J. M. Blatt and V. F. Weisskopf, *Theoretical Nuclear Physics*, 2nd ed. (Springer-Verlag, New York, 1979).

[26] D. D. Clayton, *Principles of Stellar Evolution and Nucleosynthesis*, 2nd ed. (University of Chicago Press, Chicago, 1983).

[27] Ş. Mişicu and M. Rizea, α-decay in ultra-intense laser fields, J. Phys. G **40**, 095101 (2013).

[28] H.-S. Bosch and G. M. Hale, Improved formulas for fusion cross-sections and thermal reactivities, Nucl. Fusion **32**, 611w (1992).

[29] W. M. Nevins and R. Swain, The thermonuclear fusion rate coefficient for p-^{11}B reactions, Nucl. Fusion **40**, 865 (2000).